Research Square

Preprints are preliminary reports that have not undergone peer review.
They should not be considered conclusive, used to inform clinical practice,
or referenced by the media as validated information.

An efficient and aberration-free off-plane grating spectrometer and monochromator for EUV – soft X-ray applications

Kui Li
Aerospace Information Research Institute, Chinese Academy of Sciences
Dimitar Popmintchev
TU Wien https://orcid.org/0000-0001-8203-4703
Ruixuan Li
Aerospace Information Research Institute, Chinese Academy of Sciences
Guangyin Zhang
Aerospace Information Research Institute, Chinese Academy of Sciences
Runyu Meng
Yunnan Observatories, Chinese Academy of Sciences https://orcid.org/0000-0001-6362-0707
Yongjun Ma
Aerospace Information Research Institute, Chinese Academy of Sciences, Beijing 100094, China
Hao Xu
Aerospace Information Research Institute, Chinese Academy of Sciences, Beijing 100094, China
Jiyue Tang
Aerospace Information Research Institute, Chinese Academy of Sciences, Beijing 100094, China
Changjun Ke
Aerospace Information Research Institute, Chinese Academy of Sciences, Beijing 100094, China
Jisi Qiu
Aerospace Information Research Institute, Chinese Academy of Sciences, Beijing 100094, China
Yunfeng Ma
Aerospace Information Research Institute, Chinese Academy of Sciences, Beijing 100094, China
Tenio Popmintchev
University of California San Diego https://orcid.org/0000-0002-2023-2226
Xiaoshi Zhang
Aerospace Information Research Institute, Chinese Academy of Sciences
Zhongwei Fan
Academy of Opto-Electronics, Chinese Academy of Sciences
Jie Li (lijie430@aircas.ac.cn)
Aerospace Information Research Institute, Chinese Academy of Sciences

Article

Keywords:

Posted Date: June 14th, 2023

DOI: https://doi.org/10.21203/rs.3.rs-2990431/v1

License: This work is licensed under a Creative Commons Attribution 4.0 International License.
Read Full License

Additional Declarations: (Not answered)

Version of Record: A version of this preprint was published at Light: Science & Applications on January 8th, 2024. See the published version at https://doi.org/10.1038/s41377-023-01342-9.

An efficient and aberration-free off-plane grating spectrometer and monochromator for EUV – soft X-ray applications

Jie Li[1,2], Kui Li[1,2], Dimitar Popmintchev[3], Ruixuan Li[1,2], Guangyin Zhang[1,2], Runyu Meng[4], Yongjun Ma[1], Hao Xu[1], Jiyue Tang[1,2], Changjun Ke[1,2], Jisi Qiu[1,2], Yunfeng Ma[1,2], Tenio Popmintchev[3,5], Xiaoshi Zhang[1,2] and Zhongwei Fan[1,2]

[1]*Aerospace Information Research Institute, Chinese Academy of Sciences, Beijing 100094, China*
[2]*School of Optoelectronics, University of the Chinese Academy of Sciences, Beijing 100049, China*
[3]*Photonics Institute, TU Wien, Vienna A-1040, Austria*
[4]*Yunnan Observatories, Chinese Academy of Sciences, Kunming, Yunnan 650011, China*
[5]*University of California, Physics Department, San Diego, La Jolla, CA 92093, USA*
Corresponding authors: [2] fanzhongwei@aoe.ac.cn, [1]zhangxs@aircas.ac.cn,
[5]tenio.popmintchev@physics.ucsd.edu, [3]dimitar.popmintchev@gmail.com
These authors contributed equally: Jie Li, Kui Li

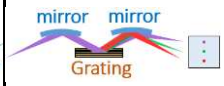
Abstract: We demonstrate a novel dual-optic imaging EUV-X-ray spectrometer and monochromator that attains an unprecedented throughput efficiency exceeding 60% theoretically, along with a superior spectral resolution of $\lambda/\Delta\lambda>200$. Exploiting the benefits of the conical diffraction geometry, the optical system is globally optimized in multidimensional parameter space to guarantee optimal imaging performance over a broad spectral range while maintaining circular and elliptical polarization states at the first, second, and third diffraction orders. Moreover, our analysis indicates minimal temporal dispersion, with pulse broadening confined within 80 fs, which enables ultrafast spectroscopic and pump-probe measurements with femtosecond accuracy. Furthermore, the spectrometer can be effortlessly transformed into a monochromator spanning the EUV–soft X-ray spectral region. Such capability allows coherent diffractive imaging applications to be conducted with highly monochromatic light in a broad spectral range and extended to the soft X-ray region with minimal photon loss. Thus, enhancing the imaging resolution and enabling the investigation of bio and nano samples. In addition, the advanced design incorporates optimized spatio-temporal parameters, facilitating cutting-edge versatile EUV - X-ray applications.

1. INTRODUCTION

Ever since the first observation of high-order harmonics (HHG) using ultrashort ultraviolet (UV) and infrared (IR) laser pulses, the extreme nonlinear upconversion phenomenon has become a practical laboratory-scale technology for producing coherent light in the EUV and soft X-ray spectral ranges exceeding keV photon energies [1-10]. In more than three decades of intense research, this light source has evolved into a versatile laser light tool extending across the EUV and soft X-ray region [1-11], with temporal bursts as short as ~40 attoseconds, potentially approaching even a few attoseconds if compressed [12]. Such light sources can pass through optically nontransparent objects, visualize subwavelength nanostructures, manipulate magnetic states and currents, and study materials' chemistry and structure at picometer and femtosecond-to-attosecond scales, etc., [10, 13-17]. In addition, the HHG sources can also be designed to have a variable spin and orbital angular momentum states like ordinary lasers [18, 19]. The advent of the kHz – MHz femtosecond laser amplifiers scaled the average high harmonic power to more than ten milliwatts [20], thus, already advancing a wide range of spectroscopic and imaging applications in the fields of physics, chemistry, and nanoscience. Furthermore, the superior spatial and temporal coherence of the harmonics, compared to other large- and small-scale sources, and their attosecond-to-femtosecond temporal and nanometer

spatial resolution has enabled dynamic studies at the space-time resolution extreme of atomic, molecular systems, advanced quantum materials, and nano-devices [21-24]. This unique light tool has recently become a commercial instrument for scientific and industrial applications [25].

Table 1 Some of the most advanced HHG spectrometers to date.

Designed function	Spectrometer	Monochromator	Spectrometer /monochromator	Spectrometer /monochromator (this work)
Schematic diagram				
Number of optics	1	6	3	2
Grating type	VLS grating [26-29]	dual plane grating using collimated beam [30, 31]	plane grating using collimated beam [32]	plane grating using focused beam
Throughput Efficiency	5% —15%	~6%	~25%	exp. average 7 HH >40% (>60% - theoretically)
Imaging mode	No	Yes	Yes	Yes
Spectral resolution ($\lambda/\Delta\lambda$)	200-1000	~100	>200	>200
Spectral range	1-100 nm (3 gratings)	25-400 nm (3 gratings)	10-50 nm (3 gratings)	10-50 nm (1 grating)
Preserves polarization	N.A.	N.A.	Yes	Yes
Temporal dispersion	~1 ps	<5 fs	~100 fs	~80 fs

In static and dynamic coherent EUV - X-ray measurements, the transmitted or reflected light is analyzed using two general approaches: an ultrabroad bandwidth EUV – X-ray illumination [33] or a monochromatic illumination. However, due to the short wavelength of the light (1 nm - 100 nm) and the strong material absorption in the EUV - SXR electromagnetic region, the optics used in a spectrometer or monochromator such as gratings, steering multilayer mirrors, focusing toroidal or elliptical mirrors typically have low throughput efficiency and high cost. Additionally, the low conversion efficiency of the HHG sources - on the order of a few microwatts or even nanowatts - further complicates experiments where the signal-to-noise ratio is of the essence. Consequently, low photon emission has been the major roadblock in HHG applications. Therefore, while developing a brighter HHG source seems to be the most apparent solution, designing highly efficient EUV - SXR spectrometer or monochromator instruments is another key to resolving such problems.

Various types of spectrometers or monochromator instruments have been developed for tabletop sources, generally consisting of focusing optics and diffraction gratings that are mainly used at grazing incidence angles. The most straightforward EUV - SXR spectrometer uses a single optic: typically, either a toroidal or cylindrical grating with either imaging-mode capability or flat field mode, but not both. The single-optic spectrometer is simple and easy to align [26, 27]. However, it suffers from either aberrated wavefront or manufacturing defects.

To circumvent such problems, multi-optics (typically three or more optical elements) spectrometers were also explored in various HHG applications [32, 34]. The focusing and diffraction functions are separated inside such spectrometers, allowing for a better spatial profile, lower pulse dispersion, and higher spectral resolution, which can be achieved simultaneously. However, more optical elements typically lead to alteration of the light polarization, lower throughput efficiency, higher complexity, and more complex alignment procedure. In recent applications, dual-optic spectrometers have been developed to include the merits of both single-optic and multi-optic spectrometers by reducing loss and complexity while improving flexibility and lowering production costs. Nevertheless, traditional dual-optic spectrometer [35] has intrinsic drawbacks: non-flat field, lack of imaging-mode capability, and low throughput efficiency due to non-compensable aberration and high losses introduced by the diffraction gratings. Furthermore, all of the spectrometer configurations mentioned above require the switching of several gratings in order to cover different spectral ranges.

In this paper, we report a novel dual-optic imaging spectrometer globally optimized in a multidimensional spatio-temporal space for high harmonic EUV and soft X-ray sources that circumvent all of the above-mentioned challenges. Our approach simultaneously combines a record-breaking high throughput efficiency, a high spectral resolution, a low temporal dispersion, and a broad spectral range coverage while preserving the polarization state in simple geometry. Furthermore, this dual-optic optical system is efficient and cost-effective, operating both as a monochromator or spectrometer and can be complementary or a replacement of the multilayer mirrors for a vast range of EUV and SXR wavelengths since the efficiency of the available mirrors is poor except for a few wavelengths.

2. Results. Systematic elimination of aberrations in the spatio-temporal domain.

Blazed gratings can achieve exceptionally high diffraction efficiency of over 90% when used in a conical diffraction geometry. One reason is that the shadowing effect is minimal at high grazing angles [36]. However, the conical geometry also introduces relatively high aberrations, which has restricted their applicability thus far in the EUV-SXR spectral region. A traditional approach uses a collimated beam to reduce the distortions caused by the grating at conical diffraction geometry. Conversely, this requires implementing at least two focusing optical elements in the spectrometer: one for collimating and one for focusing. As a result, the design becomes more complex, and the alignment is more challenging. By using more optics, such approaches also lower the throughput efficiency of the optical system. Contrary, we demonstrate here, for the first time, that we can correct the aberrations from the grating by slightly misaligning one of the tilt angles of the toroidal mirror, using only two optical elements.

In this paper, we design a globally optimized and aberration-free system using a blazed grating at conical diffraction geometry in combination with a toroidal mirror at a grazing angle, as shown in Fig. 1a. We note that the focusing optic can be any type of curved mirror forming a 2D focal spot with relatively low aberrations, i.e., elliptical mirror. A toroidal mirror has minimal aberrations when used in 1:1 imaging systems. However, when such a spectrometer is used in other than 1:1 imaging, a low aberration mirror should be preferred, i.e., elliptical mirror, diabolic, etc. We start by systematically removing the present aberrations. For that purpose, our simulations first consider the HHG light as a point source with a full divergence angle of 2θ. A toroidal mirror with an effective focal length f images the HHG source onto the CCD camera. The source and the camera are $4f$ apart. The grating is halfway between the toroid and the detector, with its grooves parallel to the Z axis. The direction of the incoming and diffracted rays on the grating can be described by two parameters: the altitude angle γ, which is the angle between the ray and the groove direction, and the azimuth angle α (or β), which is the angle

between the grating normal and the projection of the incoming (or diffracted) ray on the plane perpendicular to the grooves.

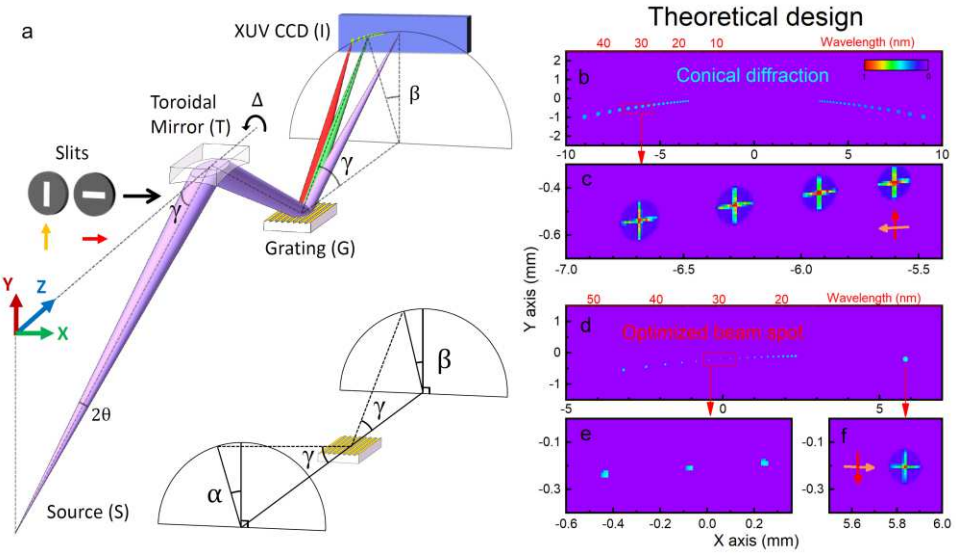


Fig. 1 Aberration-corrected spectrometer in conical diffraction geometry. The spectrometer geometry consists of a toroid mirror, free to rotate about the z-axis, and a plane conical grating. The altitude angle, γ, and the azimuth angle, α (or β), describe the direction of the incoming and diffracted rays. The horizontal and vertical slits are only for simulation models. The arrows (yellow and red) show the slits' direction, representing the signs of the aberrations from the optical elements along the tangential and sagittal directions. **b** Simulated first-order diffraction beam spot of 17-45 nm detected by XUV CCD for toroidal angle $\Delta = 0°$. **c** Zoomed-in view of the first order ($m = +1$) diffracted beam near 30 nm from **b**. The bright line shows the beam distortion from the tangential and sagittal ray fans. **d** Aberration-corrected first-order beam spot by increasing the toroidal angle Δ from 0° to 2°. The spot near X = 6mm is the zero-order beam. **e** Zoomed-in view of the first order ($m = +1$) diffracted beam near 30 nm from **d**. **f** Zoomed-in view of zero order beam from **d**.

Figure 1b shows the simulated beam spot distribution of the zero and first diffraction order of the HHG beam from $17 - 45$ nm on the CCD detector. The toroidal mirror is set at the default (minimal aberration) geometry (i.e., $\Delta = 0°$). The grating diffraction angles follow equation (1).

$$\frac{m\lambda}{d} = sin\gamma(sin\alpha + sin\beta) \tag{1}$$

, where d is the groove spacing of the grating, γ is the altitude angle, α, and β are the azimuth angles, m is the diffraction order.

We use "vector" slits along the tangential and sagittal directions in front of the optics in our raytracing model to analyze the distortions of the grating and toroidal mirror. The arrow direction and length of the "vector" slits indicate the sign and magnitude of the aberrations, respectively. We define "up" or "right" pointing arrows as positive signs of tangential and sagittal aberration, respectively. The "vector" slit at the detector plane becomes a spot whenever the aberrations are canceled. For example, when $\Delta = 0°$, the zero-order reflection beam from the grating has minimal aberrations. However, the first-order diffracted beam has aberrations proportional to the diffraction angle (Fig. 1c). On the other hand, the toroidal mirror reflection at a misaligned angle $\Delta = 2°$ introduces aberrations with a sign and amount that cancels the distortions caused by the grating, as shown in Fig. 1f. Hence, the aberrations from the toroidal mirror and diffraction grating have opposite signs (tangential and sagittal) and can cancel each other under specific configurations to achieve a near-perfect focus at the detector plane. More

details can be found in the supplementary materials (SM). We further simulate the aberrations from the toroidal mirror alone by tracing the zero-order beam from the grating, as shown in Fig. 1f. In addition, we simulate the aberrations from the grating alone by tracing the first or higher-order beam from the grating when $\Delta = 0°$. Finally, we present the aberration-free system with a misaligned toroidal mirror at an angle Δ given by equation (2).

$$\Delta = \frac{m\lambda}{4\ d\ sin\gamma} \tag{2}$$

Figure 1e shows the aberration-compensated harmonic beam near the wavelength of 30 nm (41.3 eV), where $\Delta = 2°$. For small azimuth angles, equation (2) can be simplified as:

$$4\Delta = \frac{m\lambda}{d\ sin\gamma} = \sin\alpha + \sin\beta \approx \alpha + \beta \tag{3}$$

The spectrometer configuration is simplest and fully symmetric when $\alpha = 2\Delta$ and $\beta = 2\Delta$, such that the zero-order overlap for some angle Δ with the first-order diffracted beams for $\Delta = 0°$ (Fig. 1d). Such geometries are beneficial for HHG applications. The optimization procedure can be simplified as: first, mark the location of the zero-order. Next, adjust the toroidal mirror angle Δ to align the first-order HHG beam with the marked position of the zero-order. The HHG beam near that location will be naturally free of spatial aberration. The presented technique is the basis for automated monochromators for a variety of applications.

Experimental optimization and performance of the dual optic spectrometer

The high-harmonic generation (HHG) beam from 17 nm to 41 nm is produced by focusing a commercial 1036 nm Yb: KGW laser down to 100 μm into a gas cell filled with a noble gas. Next, the copropagating infrared beam is removed using aluminum thin-film filters. Then the HH beam source is reimaged 1:1 using a gold-coated toroidal mirror.

Subsequently, the converging HH spectrum is angularly dispersed using a gold-coated blazed grating in conical diffraction geometry, placed at half the distance between the toroidal mirror and the detector.

Finally, the HH spectrum is recorded using an XUV CCD camera. A zero-order half-wave plate is used to switch between the P and S polarizations. Table 2 lists the detailed optical parameters of the spectrometer.

Table 2. Parameters of the spectrometer

Parameter	value
Toroid focus length f	400 mm
Altitude angle γ	6°
Toroid misalignment angle Δ	0° to 4°
Simulated wavelength range	17-45 nm

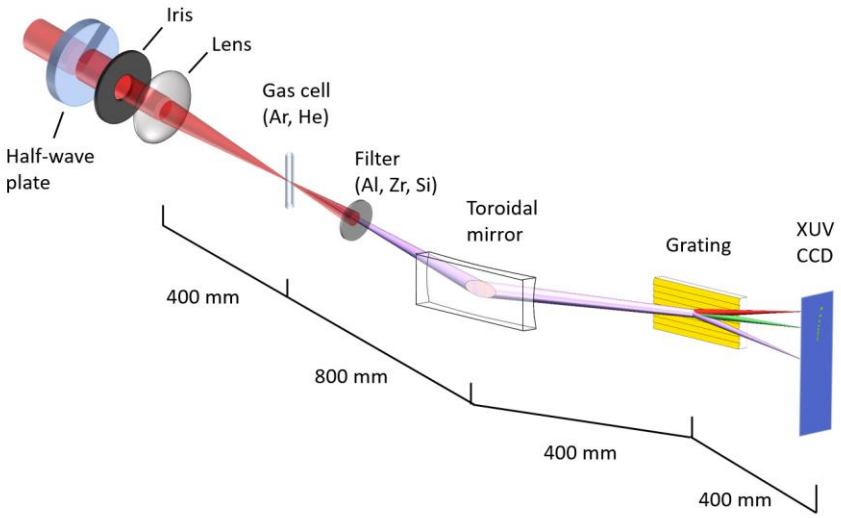


Fig. 2 Experimental setup for high harmonic spectra measurement. Schematic of the high-harmonic generation (HHG) setup. A lens with a focal length of 400 mm focuses a femtosecond laser pulse into a gas cell filled with either argon or helium gas. The generated EUV radiation is imaged by a toroidal mirror and spectrally resolved by a grating set at 6 degrees incident angle and detected by an X-ray CCD camera with 20×20 μm pixel size. The inset shows the measured EUV spectra for different gas pressures.

We minimized the spatial beam distribution at the detector plane for each HH beam to optimize the spectral resolution. This is done essentially by adjusting the toroidal azimuth angle. First, using argon as an X-ray generation medium, we observe seven high-order harmonics ranging from the 25^{th} to 37^{th} (between 28 and 41 nm) on the CCD.

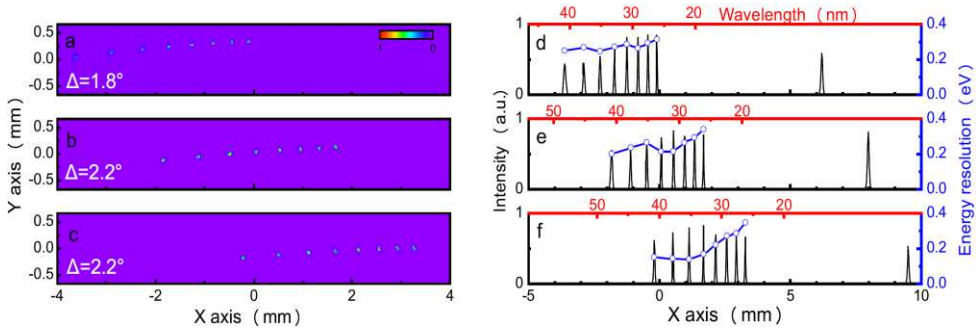


Fig. 3. Experimental optimization of spectral resolution and spatial profiles of the high-order harmonic beams. EUV spectra from the 25^{th} through 39^{th} harmonic orders recorded using an X-ray CCD camera. The spectral resolution is optimized by minimizing the focus spot sizes of the HH beam on the CCD. The angle Δ of the toroidal mirror is adjusted to relocate and refocus different harmonic beams to the center of the detector (x=0), where spatial aberrations will be compensated. The insets show perfectly round spatial profiles of the optimized 39^{th} **a**, 33^{rd} **b**, and 25^{th} **c** harmonics at Δ = 1.8°, 2.2°, 2.8°, respectively. The normalized EUV spectral intensity shows efficiency greater than 40% and energy resolution $\lambda/\Delta\lambda > 200$ at these angles (**d**-**f**). For example, in our configuration, the 25th harmonics (41 nm) in (**f**), the resolution was 0.15 eV at 30 eV.

We then adjust the angle Δ of the toroidal mirror from 0° to 1.8°, 2.2°, or 2.8° to relocate and refocus the 39^{th}, 33^{rd}, or 25^{th} harmonics in the first diffraction order to the center of the detector (Fig. 3a-c). Fig. 3 also shows the achieved excellent resolution of ~ 0.2 eV for all seven harmonics.

For example, for the 25^{th} harmonics (41 nm) in Fig. 3f, the resolution is $\lambda/\Delta\lambda \cong 200$, corresponding to 0.15 eV resolution at 30 eV in our configuration. This design can also serve as a monochromator by placing a vertical slit at $x = 0$ and choosing the correct angle Δ to select a specific wavelength with minimum aberration. A second toroidal or ellipsoidal mirror can then refocus and demagnify the monochromatic beam spot to a smaller size.

It is worth noting that the FWHM beam diameter of the 39^{th} harmonic at 26 nm (Fig. 3a) is only 3 pixels, corresponding to ~ 60 μm. Our raytracing simulation results show an optimized spot size of ~ 20 μm using a measured source divergence angle of 1.2 mrad, assuming that the signal is emitted from a point source. This is the theoretical spatial extent of the point spread function of the optical system. Nonetheless, other factors, like the surface imperfection of grating and toroid, can also contribute to the bigger beam size observed on the CCD.

One of the significant advantages of using a grating in conical diffraction geometry is its high diffractive efficiency. For a grating with blazing angle ψ, the diffraction efficiency reaches the maximum when the incident light and the diffracted light specularly reflect off the groove surface. Then the angles satisfied the following relationship:

$$\alpha + \beta = 2\psi \tag{4}$$

Another constraint that affects the diffraction efficiency is the shadowing effect for the blazed grating. If the direction of incident light is not perpendicular to the groove surface, each groove is partially illuminated due to the shadow area from the adjacent grooves. The shadowing effect can be zero when $\alpha = \psi$. According to equation (3), optimal efficiency is achieved when $\alpha = \beta = \psi$. This is also the so-called "Littrow" condition. In which the diffraction efficiency and diffracted mode quality can be further improved. It is worth noting that the shadowing effect can be neglected when ψ is small.

Figure 4a shows the calculated grating's diffractive efficiency for the P and S polarization state for the first four diffraction orders in the spectral range 5 to $50nm$, using a coupled-mode theory [37-40]. We assume ideal gold-coated surfaces with no contamination or surface roughness. The highest efficiencies are obtained at three wavelengths: 32.6 nm, 16.97 nm, and 11.3 nm. For the first-order diffraction, the maximum efficiency is 67.7% for P polarization and 73.6% for S polarization at 32.6 nm. For the second-order diffraction, the maximum efficiency is 70.6% for P polarization and 72.9% for S polarization at 16.97 nm. For the third-order diffraction, the maximum efficiency is 77% for P polarization and 77.9% for S polarization at 11.3 nm. For the first time, the first, second, and third diffractive order can be used to cover the entire spectral range from 10nm to 50nm at near-constant high efficiency with just a single grating. This was not posible in any prior design. Furthermore, Fig. 4a also shows that the grating efficiencies are very close for the S and P polarizations, especially in the short wavelength region and at small grazing angles. Hence, the spectrometer could adequately preserve the beam polarization.

To validate our theoretical optimization design, the diffractive efficiencies are measured experimentally. The experiments are first conducted at the 26 to 41 nm spectral range. The relative signal strength between the zero, first, and second-order is plotted in Fig. 4b. For spectral signals near 30 nm, the maximum diffraction efficiency falls into the first order, which agrees exceptionally well with the theoretical calculations. Next, the HH signal is measured without grating at the 26 to 41 nm spectral range to acquire the absolute diffraction efficiency. We measured the absolute grating efficiency to be 50.4% in the first order by comparing the signal with and without a grating. In excellent agreement with the experimental data, the theoretically averaged diffraction efficiency of the gold-coated grating for harmonics in the 26

to 41 nm spectral range is 61.5% for the P and 66.4% for the S polarization. It is also noted that it is possible to further increase the absolute diffraction efficiency by using a smaller grazing angle geometry without modifying the geometry of the spectrometer.

The efficiencies of the HH beam with P and S polarization are measured by changing the driving laser polarization with a half-wave plate. The experimental and theoretical data suggest that the difference between the s- and p- polarization signal strength is less than 10% in the EUV and significantly decreases towards the soft X-ray region, Fig 4a and FigS1 (SM). Thus, this spectrometer scheme is ideal for preserving the circular polarization state or angular momentum of the HHG beam.

The spectrometer's wide tunability is verified by recording harmonic spectra generated in helium gas in the 17-33 nm spectral range. A larger misalignment angle $\Delta=3°$ is used to optimize the spectral focus. The relative signal strength between the zero, first, and second order are plotted in Fig. 4c. Consistent with our theoretical curve (red) in Fig. 4a, the second-order diffractive signal peaked at 17.6 nm. By minimizing the aberration of the HH order at 17.6 nm (71 eV), an energy resolution of 0.34 eV is achieved, corresponding to a relative resolution of $\lambda/\Delta\lambda=209$.

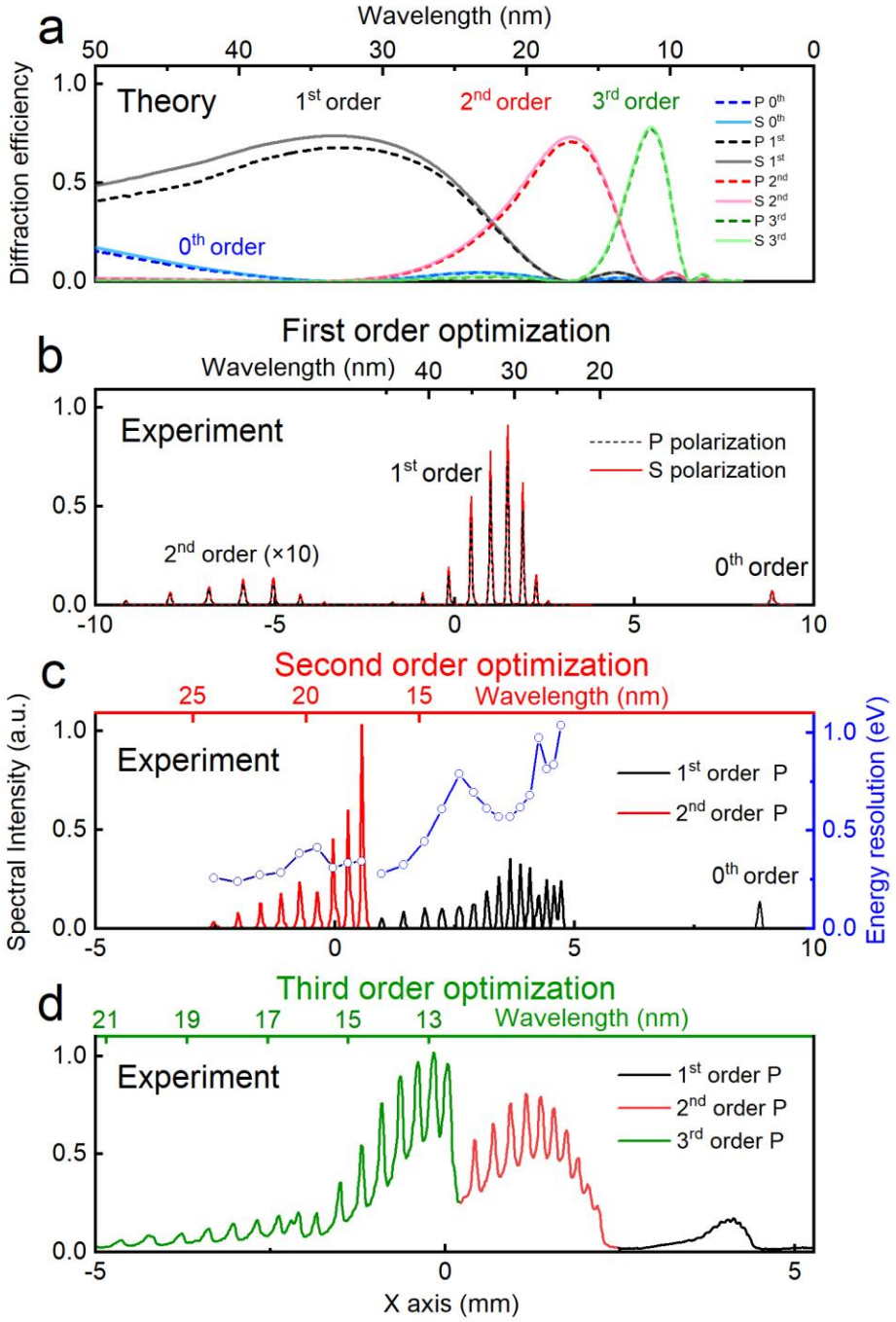


Fig. 4 Efficiency and resolution in the first, second, and third-order diffraction. a An absolute grating efficiency from coupled-mode simulation of the s and p polarizations in conical geometry. The solid and dashed lines represent the S and P polarizations, respectively. **b** Experimental data of high harmonics covering 26-41 nm in the zero, first, and second order. **c** Experimental data of p-polarized high harmonics covering 17-33 nm spectral range in the zero, first, and second (red line) order and its corresponding energy resolution (blue dot). **d** Experimental data of p-polarized high harmonics covering 12-20 nm spectral range in the first, second, and third (green line) order.

To verify the extreme performance of third-order diffraction, we use high harmonics in the $12-20$ nm spectral range filtered with silicon thin-film foils. The relative signal strength between the first, second, and third order are plotted in Fig. 4d. For signal near the silicon edge (~12 eV), the highest diffraction efficiency goes into the third-order. This agrees well with our theoretical curve (green) in Fig. 4a. The reduced spectral resolution near 13 nm is caused by spectrum overlapping between second and third-order signals, which can be corrected computationally.

Further, the spectrometer has theoretical throughput above 60% in the first, second, and third order, Fig S1 (SM). The plotted data results from 2000 Monte Carlo raytracing simulations of the optical system for an energy interval of $E/dE = 200$, with source parameters as described in the next section. For the first-order diffraction, the maximum throughput efficiency is 49.8% for P polarization and 61.3 % for S polarization at 33 nm. For the second-order diffraction, the maximum throughput efficiency is 53.2% for P polarization and 58.7% for S polarization at 17 nm. Finally, for the third-order diffraction, the maximum throughput efficiency is 63.3% for P polarization and 65.2 % for S polarization at 11.3 nm. Moreover, an advantage of the presented spectrometer is that the zero-order intensity is less than the higher orders, allowing simultaneous observation on an X-ray CCD camera.

As a result, the first, second, and third orders, etc., from a single grating can be exploited in spectrometer design. A similar rule should apply to even higher orders. For example, one could cover a broad-spectrum range with the highest resolution by selecting the diffraction order with the highest efficiency and optimizing the corresponding toroidal angle.

Temporal characteristics of the dual-optic spectrometer

An essential application of high-order harmonic sources is studying ultrafast dynamics in materials, nanostructures, magnetic and quantum materials, etc. In such applications, maintaining the high-order harmonic pulse duration is of the essence when transmitting the HHG beam through multiple optical elements, i.e., spectrometers, monochromators, etc. Diffraction gratings introduce a fair amount of spatial and temporal distortions that can drastically increase the pulse duration width. Pulse broadening caused by the chromatic dispersion of complex optical systems is often analyzed using a perturbative approach – the Lah-Laguerre optical formalism (LLOF).[41-43]. In the case of a single grating, the broadening $\Delta\tau$ is mainly due to the pulse front tilt, as shown in Fig. 5a [44].

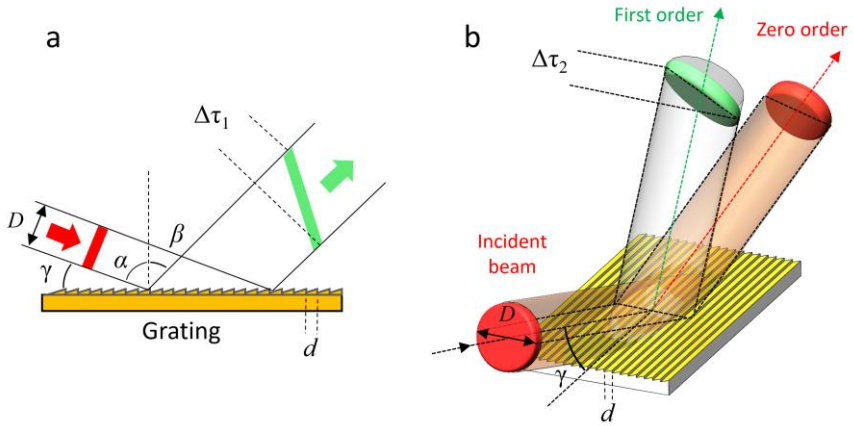


Fig. 5 Temporal broadening of the diffracted beam caused by pulse front tilt. a Normal diffraction geometry. **b** Conical diffraction geometry. $\Delta\tau$ is pulse broadening caused by pulse front tilt, D is the diameter of the incident beam,

d is the grating groove spacing, N is the total number of grooves illuminated within the beam diameter, γ is the beam grazing angle, c is the speed of light and λ is the wavelength.

The broadening is proportional to the total number of groves N_1 illuminated within the beam diameter D, and will increase with the decrease of the grazing angle γ. In the case of conical diffraction shown in Fig. 5b, for $\gamma \ll 1$, the total number of groves N_2 illuminated is irrelevant of grazing angle γ, resulting in less pulse broadening when compared to the normal grating geometry. To quantitatively assess the pulse characteristics of our system, we employed Monte-Carlo ray tracing, which efficiently characterizes both spatial and temporal beam parameters in a very computationally efficient manner with a relatively small number of rays. Our simulation utilized a fully coherent statistical source at 29.9 nm (41.4 eV), with a flat top spectrum of ± 0.15 nm, 30 μm standard deviation spatial width extent (with beam spot ellipsoid parameters a =70.06 μm, b = 69.55 μm, measured at 2σ), and a statistical divergence of 1.2 mrad standard deviations. In addition, we optimized the system's geometry with a tilted toroid near 2º to minimize any temporal aberrations at this specific wavelength. In the temporal domain, a plane wave beam is broadened by the spectrometer to 11.87 fs standard deviation and spans nearly 80 fs tail to tail, as shown in Fig. 6b. The ray tracing beam spot diagram in Fig. 6a displays the distortion-corrected, spatial beam spot distribution at focus. The ellipsoid parameters, measured at 2σ, are a = 81.6 μm and b = 70.63 μm at focus, representing 1:1 imaging despite the presence of the aberrations from the dispersive element and the tilted toroid. The spectrometer/monochromator under these conditions has a theoretical wavelength resolution of 5 nm/mm . Our approach of using Monte-Carlo ray tracing and optimizing system geometry allowed us to efficiently evaluate the temporal characteristics of the system and minimize temporal aberrations at a specific wavelength.

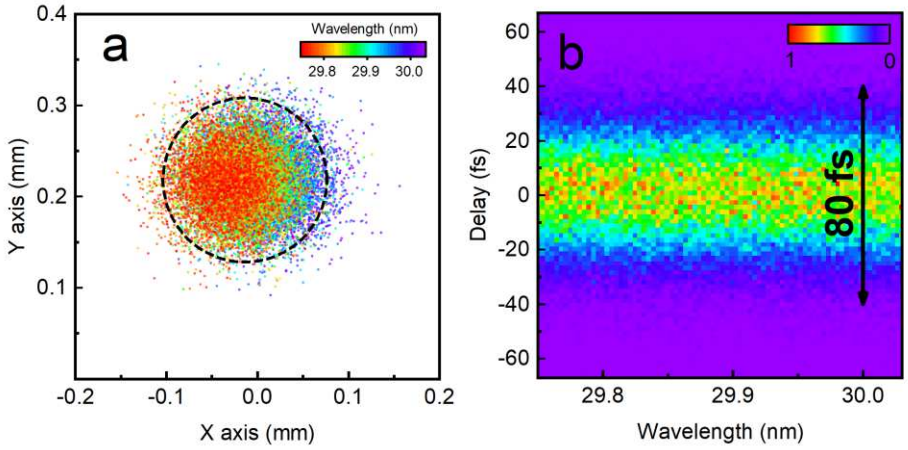


Fig. 6 Temporal spread of the diffracted beam in the first diffraction order of the optimized monochromator. a Monte-Carlo ray tracing of a single harmonic at 29.9 ± 0.15 nm with color-encoded wavelength distribution at the exit of the slitless monochromator with aberration correction by tilting the toroid by an angle $\Delta = 2.05°$. The dashed elliptical line shows the 2σ confidence interval. **b** Extracted temporal pulse broadening from Monte-Carlo ray tracing. The broadening is mainly caused by pulse front tilt with a standard deviation of 11.87 fs and an edge-to-edge spanning of nearly 80 fs.

Furthermore, because the amount of broadening is proportional to the laser beam size on the grating, in our spectrometer design, one can vary the distance between the focusing mirror and the grating. As a result, the beam size on the grating will change correspondingly, resulting in an adjustable pulse width at the focus of the CCD plane. Thus, as shown in Fig. 7, we investigate the impact of the distortions introduced by the grating at various distances in our raytracing model.

As outlined in Section 2, the CCD records the beam aberrations that result from both the toroidal surface reflection and the grating diffraction dispersion. The amount of toroidal distortions is proportional to the misaligned angle Δ and the propagation distance from toroidal to CCD (see equation S3 in SM). While the distortions from the conical diffraction are proportional to the angle of diffraction $\alpha + \beta$ and the propagation distance from grating to CCD (see equation S1 in SM), as a result, the optimized beam is located at the center of the CCD (see Fig. 7) even if the grating is not centered in between the toroidal and CCD.

$$\frac{\alpha}{\beta} = \frac{GI}{TG} \tag{5}$$

$$\frac{\alpha + \beta}{4\Delta} = \frac{ST}{2GI} \tag{6}$$

Since $\alpha = 2\Delta$, we then have:

$$\alpha = 2\Delta \tag{7}$$

$$\beta = 2\Delta \frac{TG}{GI} \tag{8}$$

For condition (b) in Fig. 7, we have $ST = 2TG = 2GI$ (see Fig. 7b), which leads to $\alpha + \beta = 4\Delta$, consistent with equation (3).

Considering the finite size and pixel density of commercial X-ray CCD, our spectrometer scheme can operate at a high spectral resolution (Fig. 7a) by increasing the grating to CCD distance (GI). However, the consequence is more significant temporal pulse broadening. Alternatively, by decreasing the distance GI (Fig. 7c), we can reduce the temporal pulse broadening and increase the spectral record range.

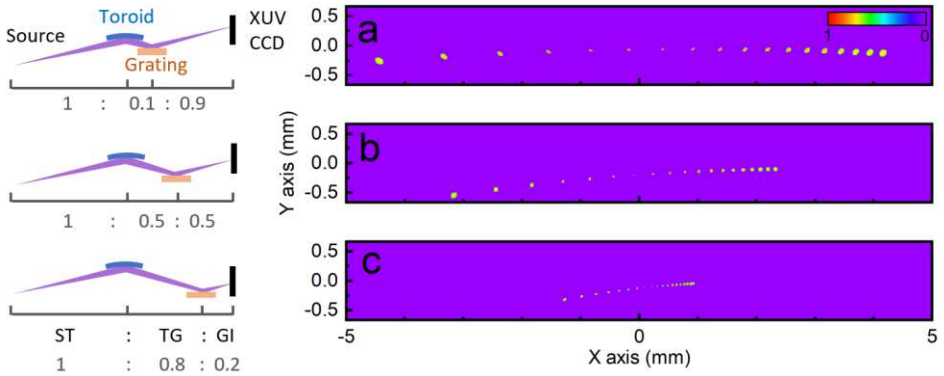


Fig.7 Tunable spectrometer resolution and tunable pulse broadening through the toroid-grating distance. The spectrometer's spectral resolution and the temporal pulse broadening can be varied by adjusting the distance GI between the grating and the CCD. A larger GI gives a higher resolution but also a more significant pulse broadening. Conversely, a smaller GI offers a lower resolution but also a smaller broadening in a wider spectral range. The angle Δ in **a**, **b,** and **c** equals 3.6°, 2.0°, and 0.8°, respectively.

3. Summary

In summary, we have developed a highly-efficient imaging spectrometer with exceptional performance characteristics. By using a conical diffraction geometry with a single toroidal mirror and a single grating, we measure a throughput efficiency of more than 40%. Furthermore, the theoretical throughput efficiency for a system free of imperfections, such as surface

roughness and contamination, surpasses 60% in all orders. The high throughput efficiency is also accompanied by a superior spectral resolution of $\lambda/\Delta\lambda > 200$, over a broad spectral range between 17 nm and 41 nm or 30 eV - 73 eV, which can be extended even further into the soft X-ray range.

One of the key advantages of our design is that it compensates for spatial aberrations of the selected harmonic beam caused by the conical diffraction grating with a simple azimuthal rotation of the toroidal focusing mirror relative to the grating. This approach ensures optimal imaging performance over a broad spectral range while maintaining circular and elliptical polarization states at the first, second, and third diffraction orders.

Furthermore, our analysis indicates minimal temporal dispersion, with pulse broadening confined within 80 fs. This level of performance enables unprecedented ultrafast spectroscopic and pump-probe experiments with attosecond-to-femtosecond precision, providing researchers with a powerful tool for studying a wide range of phenomena in the X-ray and EUV spectral regions.

In addition to its exceptional imaging and spectroscopic capabilities, our spectrometer can be effortlessly converted into a monochromator that covers the 20-70 eV range and beyond. This makes it ideal for coherent diffractive imaging applications that require highly monochromatic light in a broad and tunable wavelength range. In such a way, the monochromator can extend the capabilities of the CDI to the soft X-ray region with minimal photon loss, enabling unprecedented imaging resolution for bio and nano samples that can be investigated in depth.

Finally, our understanding of the physical optical phenomena related to imaging distortions has resulted in the design of an instrument with optimized spatio-temporal parameters, facilitating advanced and versatile X-ray and EUV measurements. This robust and practical design is ideal for use in both lab-scale coherent sources as well as next-generation attosecond EUV – X-ray sources at large-scale laser facilities [45]. Our work opens up exciting new possibilities for a wide range of scientific investigations, from fundamental studies of matter to applied research in areas such as materials science, chemistry, and biology.

4. Materials and method. Laser system and high-order harmonic generation

The high-harmonic signals in the extreme ultraviolet (XUV) range are generated using two different laser sources and gas targets. For the signal from 17 nm to 41 nm shown in Fig 3 and Fig 4b, c, we use a commercial 1036 nm, 200 fs Yb: KGW 6W laser (PHAROS, Light conversion) with pulse energy up to 1.5 mJ. We focus the laser beam to a diameter of 100 μm using a 400 mm focal length lens. We place a gas cell near the focus for laser-gas interaction. We use argon gas and aluminum filters to maximize the signal in the range of 25 nm to 41 nm shown in Fig 3 and Fig 4b. In addition, we use helium gas to allow higher phase-matched laser intensity and generate a signal in the range of 17 nm to 25 nm shown in Fig 4c.

The signal from 12 nm to 20 nm shown in Fig 4c, is generated using an 800nm,30fs Ti: sapphire laser with pulse energy up to 3 mJ. We first focus the laser beam to a diameter of 150 μm using a 400 mm focal length lens. Next, we use helium gas to generate a high-harmonic signal in the 12 nm to 20 nm range shown in Fig 4c.

Acknowledgments

J.L., X.Z. and Z.F. gratefully acknowledge funding from the National Key Research and Development Program of China (2021YFB3602600); the Chinese Academy of Sciences (CAS) (GJJSTD20200009) (2018-131-S); the National Natural Science Foundation of China (NSFC) (62121003) (10010108B1339-2451) and the Beijing Municipal Science & Technology Commission (Z221100006722008). In addition, T.P. gratefully acknowledges funding from the

European Research Council (ERC) (grant agreement XSTREAM-716950); the Alfred P. Sloan Foundation (FG-2018-10892).

Author contributions

J.L., K.L. and X.Z. (in cooperation with R.L., G.Z. and R.M.) prepared and performed the experiment. J.L., D.P., and T.P. globally optimized and designed the systems in multidimensional parameter space to maximize efficiency and minimize spatio-temporal aberrations. J.L., X.Z., D.P. and T.P. wrote major parts of the manuscript. All authors commented and discussed this work.

Supplementary information

Supplementary information is available in the online version of the paper.

Conflict of interest

The authors declared no conflicts of interest.

References

1. McPherson, A., et al., *Studies of multiphoton production of vacuum-ultraviolet radiation in the rare gasses.* Journal of the Optical Society of America B, 1987. **4**: p. 595-601.
2. Li, X.F., et al., *Multiple-Harmonic Generation in Rare Gases at High Laser Intensity.* Physical Review A, 1989. **39**: p. 5751-5761.
3. Krause, J.L., K.J. Schafer, and K.C. Kulander, *High-order harmonic generation from atoms and ions in the high intensity regime.* Physical Review Letters, 1992. **68**(24): p. 3535-3538.
4. Corkum, P.B., *Plasma perspective on strong field multiphoton ionization.* Physical review letters, 1993. **71**(13): p. 1994.
5. Tamaki, Y., K. Midorikawa, and M. Obara. *Phase-matched third-harmonic generation in a gas-filled hollow waveguide*. in *Lasers and Electro-Optics Society Annual Meeting, 1997. LEOS '97 10th Annual Meeting. Conference Proceedings., IEEE*. 1997.
6. Rundquist, A., et al., *Phase-matched generation of coherent soft X-rays.* Science, 1998. **280**(5368): p. 1412-1415.
7. Chang, Z.H., et al., *Generation of coherent soft x rays at 2.7 nm using high harmonics (vol 79, pg 2967, 1997).* Physical Review Letters, 1998. **80**(8): p. 1795-1795.
8. Popmintchev, T., et al., *Enhanced high harmonic generation in xe, kr and ar using a capillary discharge.* Conference on Lasers and Electro-Optics/Quantum Electronics and Laser Science Conference and Photonic Applications Systems Technologies, page JFA3. Optical Society of America, 2007.
9. Popmintchev, T., et al., *Bright coherent ultrahigh harmonics in the keV x-ray regime from mid-infrared femtosecond lasers.* science, 2012. **336**(6086): p. 1287-1291.
10. Popmintchev, D., et al., *Ultraviolet surprise: Efficient soft x-ray high-harmonic generation in multiply ionized plasmas.* Science, 2015. **350**(6265): p. 1225-1231.
11. Chen, M.-C., et al., *Generation of bright isolated attosecond soft X-ray pulses driven by multicycle midinfrared lasers.* Proceedings of the National Academy of Sciences, 2014. **111**(23): p. E2361-E2367.
12. Gaumnitz, T., et al., *Streaking of 43-attosecond soft-X-ray pulses generated by a passively CEP-stable mid-infrared driver.* Optics Express, 2017. **25**(22): p. 27506-27518.
13. Zutic, I., J. Fabian, and S. Das Sarma, *Spintronics: Fundamentals and applications.* Reviews of Modern Physics, 2004. **76**(2): p. 323-410.
14. Miao, J., et al., *Beyond crystallography: Diffractive imaging using coherent x-ray light sources.* Science, 2015. **348**(6234): p. 530-535.
15. Zhang, B., et al., *High contrast 3D imaging of surfaces near the wavelength limit using tabletop EUV ptychography.* Ultramicroscopy, 2015. **158**: p. 98-104.
16. Adams, D.E., et al., *A generalization for optimized phase retrieval algorithms.* Optics Express, 2012. **20**(22): p. 24778-24790.
17. Popmintchev, D., et al., *Near- and Extended-Edge X-Ray-Absorption Fine-Structure Spectroscopy Using Ultrafast Coherent High-Order Harmonic Supercontinua.* Physical Review Letters, 2018. **120**(9): p. 093002.
18. Klemke, N., et al., *Polarization-state-resolved high-harmonic spectroscopy of solids.* Nature Communications, 2019. **10**(1): p. 1319.

19. Kfir, O., et al., *Generation of bright phase-matched circularly-polarized extreme ultraviolet high harmonics.* Nature Photonics, 2015. **9**(2): p. 99-105.
20. Klas, R., et al., *Ultra-short-pulse high-average-power megahertz-repetition-rate coherent extreme-ultraviolet light source.* PhotoniX, 2021. **2**(1): p. 4.
21. Kraus, P.M., et al., *The ultrafast X-ray spectroscopic revolution in chemical dynamics.* Nature Reviews Chemistry, 2018. **2**(6): p. 82-94.
22. Li, J., et al., *Attosecond science based on high harmonic generation from gases and solids.* Nature Communications, 2020. **11**(1): p. 2748.
23. Cavalieri, A.L., et al., *Attosecond spectroscopy in condensed matter.* Nature, 2007. **449**(7165): p. 1029-1032.
24. Miao, J., et al., *Beyond crystallography: Diffractive imaging using coherent x-ray light sources.* Science, 2015. **348**(6234): p. 530-535.
25. Zhang, X., et al., *A tabletop coherent EUV source for commercial EUVL metrology and imaging applications*. SPIE Advanced Lithography. Vol. 10583. 2018: SPIE.
26. Koike, M., T. Yamazaki, and Y. Harada, *Design of holographic gratings recorded with aspheric wave-front recording optics for soft X-ray flat-field spectrographs.* Journal of Electron Spectroscopy and Related Phenomena, 1999. **101-103**: p. 913-918.
27. Nakano, N., et al., *Development of a flat-field grazing-incidence XUV spectrometer and its application in picosecond XUV spectroscopy.* Applied Optics, 1984. **23**(14): p. 2386-2392.
28. Locher, R., et al., *Versatile attosecond beamline in a two-foci configuration for simultaneous time-resolved measurements.* Review of Scientific Instruments, 2014. **85**(1): p. 013113.
29. Hilbert, V., et al., *A compact, turnkey, narrow-bandwidth, tunable, and high-photon-flux extreme ultraviolet source.* AIP Advances, 2020. **10**(4): p. 045227.
30. Frassetto, F., P. Villoresi, and L. Poletto, *Optical concept of a compressor for XUV pulses in the attosecond domain.* Optics Express, 2008. **16**(9): p. 6652-6667.
31. Eckstein, M., et al., *Alignment and characterization of the two-stage time delay compensating XUV monochromator.* arXiv: Instrumentation and Detectors, 2016.
32. Pascolini, M., et al., *Gratings in a conical diffraction mounting for an extreme-ultraviolet time-delay-compensated monochromator.* Applied Optics, 2006. **45**(14): p. 3253-3262.
33. Wang, H., et al., *Attosecond Time-Resolved Autoionization of Argon.* Physical Review Letters, 2010. **105**(14): p. 143002.
34. Sie, E.J., et al., *Time-resolved XUV ARPES with tunable 24–33 eV laser pulses at 30 meV resolution.* Nature Communications, 2019. **10**(1): p. 3535.
35. Poletto, L., et al., *Instrumentation for analysis and utilization of extreme-ultraviolet and soft x-ray high-order harmonics.* Review of Scientific Instruments, 2004. **75**(11): p. 4413-4418.
36. Cash, W., *Echelle spectrographs at grazing incidence.* Applied Optics, 1982. **21**(4): p. 710-717.
37. Derrick, G.H., et al., *Crossed gratings: A theory and its applications.* Applied physics, 1979. **18**(1): p. 39-52.
38. Greffet, J.-J., C. Baylard, and P. Versaevel, *Diffraction of electromagnetic waves by crossed gratings: a series solution.* Optics Letters, 1992. **17**(24): p. 1740-1742.
39. Bräuer, R. and O. Bryngdahl, *Electromagnetic diffraction analysis of two-dimensional gratings.* Optics Communications, 1993. **100**(1): p. 1-5.
40. Johnson, K.C., *Projection operator method for biperiodic diffraction gratings with anisotropic/bianisotropic generalizations.* Journal of the Optical Society of America A, 2014. **31**(8): p. 1698-1709.
41. Popmintchev, D., et al., *Dispersion Orders of Various Materials*, in *Optics Express*. 2022.
42. Popmintchev, D., et al., *Analytical Lah-Laguerre optical formalism for perturbative chromatic dispersion.* Optics Express, 2022. **30**(22): p. 40779-40808.
43. Popmintchev, D., et al., *Theory of the Chromatic Dispersion, Revisited.* arXiv preprint arXiv:2011.00066, 2020.
44. Poletto, L., P. Villoresi, and F. Frassetto, *Diffraction gratings for the selection of ultrashort pulses in the extreme-ultraviolet.* Advances in Solid-State Lasers: Development and Applications. INTECH, Croatia, 2010: p. 413-438.
45. Sergei, K., et al., *The ELI-ALPS facility: the next generation of attosecond sources.* Journal of Physics B: Atomic, Molecular and Optical Physics, 2017. **50**(13): p. 132002.

Supplementary Files

This is a list of supplementary files associated with this preprint. Click to download.

- 20230527Supplimentary.pdf